coatings

MDPI

Article

Characterization of Nanoporous Copper Using Scanning Probe Techniques

Stefan R. Anton [1], Denis E. Tranca [1], Stefan G. Stanciu [1], Radu Hristu [1], Cosmin K. Banica [2], Eugeniu Vasile [3], Zhaoyi Hu [4], Engang Fu [4,*] and George A. Stanciu [1,*]

[1] Center for Microscopy-Microanalysis and Information Processing, National University for Science and Technology Politehnica of Bucharest, 060042 Bucharest, Romania; antonstefan000@gmail.com (S.R.A.); denis.tranca@physics.pub.ro (D.E.T.); sgstanciu@gmail.com (S.G.S.); radu.hristu@upb.ro (R.H.)
[2] Faculty of Electrical Engineering, National University for Science and Technology Politehnica of Bucharest, 060042 Bucharest, Romania; cosmin.banica@upb.ro
[3] Department of Science and Engineering of Oxide Materials and Nanomaterials, Faculty of Chemical Engineering and Biotechnologies, National University for Science and Technology Politehnica of Bucharest, 060042 Bucharest, Romania
[4] State Key Laboratory of Nuclear Physics and Technology, School of Physics, Peking University, Beijing 100871, China; zyhu1@pku.edu.cn
* Correspondence: efu@pku.edu.cn (E.F.); stanciu@physics.pub.ro (G.A.S.); Tel.: +86-10-62750612 (E.F.); +40-214092110 (G.A.S.)

Abstract: This study explores the mechanical and optical properties of nanoporous copper (NPC) films dealloyed in acid and base using qualitative and quantitative measurements. Two types of NPC films (NPC 1 and NPC 2) were prepared by dealloying precursor films in different corrosive solutions. The films were characterized using atomic force microscopy (AFM) and scattering scanning near-field optical microscopy (s-SNOM). The AFM analysis revealed distinct nanoporous structures in both films, with NPC 2 showing larger pore sizes and the presence of copper aggregations on the surface. Rugosity measures showed that NPC 2 had higher rugosity than NPC 1 and indicated fundamental differences in the height distributions of the surface nano-topography. The Minkowski connectivity analysis highlighted differences in connectedness and topological characteristics between the two samples. The analysis of the GLCM features showed clear distinctions in ASM, Contrast, Dissimilarity, Energy, and Homogeneity between NPC 1 and NPC 2. The s-SNOM results demonstrated altered optical properties, with NPC 1 showing higher contrast at 1550 nm, while NPC 2 exhibited reversed-phase contrast at 561 nm. The phase contrast at 638 nm indicated a red-shifted optical absorption peak in NPC 2 compared to NPC 1.

Keywords: nanoporous copper; atomic force microscopy; scattering scanning near-field optical microscopy; statistical analysis; nanomaterials; copper nanostructures

check for updates

Citation: Anton, S.R.; Tranca, D.E.; Stanciu, S.G.; Hristu, R.; Banica, C.K.; Vasile, E.; Hu, Z.; Fu, E.; Stanciu, G.A. Characterization of Nanoporous Copper Using Scanning Probe Techniques. *Coatings* **2023**, *13*, 1908. https://doi.org/10.3390/coatings13111908

Academic Editor: Panos Poulopoulos

Received: 2 October 2023
Revised: 31 October 2023
Accepted: 3 November 2023
Published: 7 November 2023

Copyright: © 2023 by the authors. Licensee MDPI, Basel, Switzerland. This article is an open access article distributed under the terms and conditions of the Creative Commons Attribution (CC BY) license (https://creativecommons.org/licenses/by/4.0/).

1. Introduction

Nanoporous metals (NPMs) represent a fascinating realm of material science that has captivated the attention of researchers for a multitude of applications, each with its unique set of challenges and requirements. In this multifaceted field, the synthesis and exploration of nanoporous metals, particularly nanoporous copper (NPC), have yielded outcomes with wide-ranging implications.

One of the primary arenas where NPMs have found a pivotal role is in energy storage [1,2]. The soaring demand for efficient and high-capacity energy storage solutions has driven extensive investigations into NPMs. Their defining characteristics, including an exceptionally large specific surface area and the capacity for tunable porosity [3], make them promising candidates for catalysis [4,5] and as substrates for high enhancement factor (EF) in surface-enhanced Raman scattering spectroscopy (SERS) [6,7].

In the case of SERS, the choice of substrate is critical, as it directly affects the quality of signal amplification. Remarkably, research has illuminated the limitations of NPC in this context, where its EF has been deemed mediocre, and concerns about poor chemical stability have arisen [3]. However, researchers have not been deterred by these challenges. Notably, methods involving Cu-ion irradiation and Au-ion irradiation have led to breakthroughs. In the former, Cu-ion irradiation results in a remarkable 5-fold increase in EF compared to unirradiated NPC [6]. What is particularly intriguing is that the enhancement in SERS is solely attributed to changes in the physical characteristics of the microstructure, as only Cu ions were employed during the irradiation process. Building on this success, the latter approach involving Au-ion irradiation has demonstrated an even more astounding 10-fold improvement in the SERS effect compared to the unirradiated NPC [7]. In this instance, the enhancement is postulated to arise from a combination of physical and chemical alterations within the NPC microstructure. These findings unveil exciting possibilities for achieving exceptional signal enhancement, while also highlighting the potential of precisely tuning NPMs for specific applications.

On the catalysis front, NPMs, including nanoporous gold, have been a focal point of research due to their remarkable properties, such as a vast surface area, minimal absorption, and non-toxicity. The use of nanoporous gold in the form of a nanorod array, for instance, has demonstrated not only excellent photocatalytic activity but also long-term stability in the process of water splitting [8], a pivotal reaction in renewable energy production. These developments herald a new era in harnessing the potential of NPMs to drive the innovation of clean energy technologies, especially in hydrophilic surface coating [9].

While NPC has been the subject of extensive investigation regarding its mechanical [10] and electrical properties [11], it is worth noting that, apart from plasmonic characteristics [12], optical properties have not received as much attention. This presents a compelling avenue for exploration, as understanding the optical properties of NPC films can pave the way for diverse applications, including sensors, imaging devices, and more.

Our study builds upon preliminary investigations and the wealth of existing knowledge. It seeks to delve deeper into the profound relationship between the choice of dealloying agent and the ensuing mechanical and optical properties of nanoporous copper films. We anticipate that films dealloyed using distinct agents, such as H_2SO_4 and NaOH, will exhibit pronounced variations in pore size, surface topography, rugosity, fractal dimension, correlation length, and optical properties, encompassing reflectivity and absorption. These disparities are expected to arise from differences in the degree of dealloying, the formation of surface structures, grain and ligament development, and plasmonic effects [13].

Crucially, we hypothesize that a systematic comparison of these properties among differently dealloyed NPC films will not only provide a comprehensive understanding of the effects of dealloying agents on the resulting nanoporous structure but will also serve as a cornerstone for tailoring NPC films for specific applications. By fine-tuning the dealloying process, we anticipate that enhanced control over the mechanical and optical properties of NPC films will be attainable. This, in turn, can open doors to an array of applications that require precisely tailored materials.

The significance of our work is underscored by the pressing need to unravel the intricate relationship between dealloying agents and the ensuing mechanical and optical properties of nanoporous copper films. The implications of our research extend beyond the immediate application in material science. They hold the potential to illuminate fundamental principles governing the behavior of nanoporous materials, thereby advancing the broader understanding of these versatile materials.

Furthermore, our findings are poised to offer invaluable guidance for the design and development of NPC films with properties finely tuned for various applications, from energy storage to catalysis, and SERS. This multidisciplinary approach not only furthers the frontiers of materials science but also directly addresses the global challenges we face in energy, catalysis, and beyond, making it a pivotal step towards a more sustainable and technologically advanced future.

2. Materials and Methods

2.1. NPC Sample Preparation

The preparation of nanoporous copper films mainly consists of two steps: the preparation of the precursor films and chemical dealloying process.

Firstly, Cu–Al alloy precursor films with the thickness of 1 μm were prepared on Si (100) substrates by direct current (DC)magnetron co-sputtering using the target materials consisted of Cu target (99.99%) and Al target (99.99%). The atom ratio of $Cu_{25}Al_{75}$ precursor films was selected given the relatively uniform porosity of the finally dealloyed NPC films in different dealloying solutions. In the proper ratio of Cu–Al precursor films, the continuous dissolution of the Al element and the self-recombination of Cu atoms contributed to the formation of open-porous structure after dealloying. In order to achieve the designed copper–aluminum ratio, the deposition rate of the Cu target was selected as 0.1 nm/s, and the deposition rate of the Al target was fixed at 0.3 nm/s. Before deposition, the Si substrates were cleaned successively with hydrofluoric acid solution and anhydrous ethanol to remove the oxides and dust on the substrate surfaces and keep the surfaces clean, and the base pressure of the reaction chamber was lower than 10^{-4} Pa. During the process of co-deposition, Argon was kept flowing into the chamber at a flow rate of 50 sccm, and the argon partial pressure was kept at 1.8 Pa. The substrates were rotated at the speed of 20 rpm to ensure the homogeneity of the thin films. The substrate temperature was kept at ambient temperature during sputtering.

Secondly, chemical dealloying of the $Cu_{25}Al_{75}$ precursor films was then performed separately in H_2SO_4 aqueous solutions and NaOH aqueous solutions to obtain the NPC films (denoted as NPC 1 and NPC 2) with different structures. In addition to the influence of precursor alloy films, the corrosion liquid in the dealloying process also introduced an important effect on the microstructure of the finally prepared nanoporous copper films. Therefore, both the acid solution and base solution were selected given the varied degrees of corrosion on different phase components in the Cu–Al precursor. The proper dealloying time and concentration of dealloying solutions were confirmed experimentally in order to obtain the uniform porous structure throughout the entire 1 μm thickness of the NPC films. To be specific, both the 2 mol/L H_2SO_4 acid and the 0.5 mol/L NaOH base solution dealloying experiments were implemented at room temperature and for the same 120 min when the dealloying process had just finished. A longer dealloying time was required when the film thickness was thicker or the concentration of the corrosion solution was lower. Besides, isolating oxygen was of vital importance during the whole sample preparation process. All the dealloying experiments above were carried out in Petri dishes tightly sealed by parafilm to isolate from the air for the purpose of avoiding oxidation. Furthermore, when achieving the desired etching time, the samples were rinsed in deionized water and dehydrated alcohol several times and then dried in nitrogen gas flow to remove the residue chemical substances and avoid potential oxidation.

2.2. Characterization Techniques

The samples described above were investigated using Atomic Force Microscopy (AFM) and scattering Scanning Near-field Optical Microscopy (s-SNOM). The surface topography was examined using an NX10 Park (Suwon, Republic of Korea) equipped with a contact probe (CONTSCR, NanoWorld, Neuchâtel, Switzerland) with a tip radius of less than 10 nm and a force constant of 0.2 N/m. The acquired images were further used for quantitative measurements and analysis.

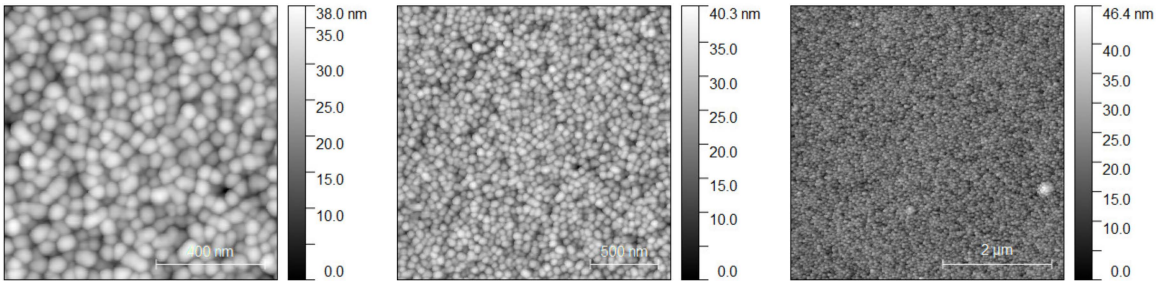
Near-field optical imaging was performed using a system produced by Nea-SNOM, Neaspec (Munich, Germany), operating in pseudo-heterodyne mode. We used three laser lines for the investigations: one in the near-infrared domain (1550 nm, laser produced by Toptica, Munich, Germany) and two in the visible range (638 nm and 561 nm, available using a laser combiner produced by Omicron, Rodgau-Dudenhofen, Germany). The cantilever used for s-SNOM investigations was a Pt-coated probe with a tip radius smaller than 35 nm, resonance frequency of 75 kHz, and force constant of 2.8 N/m (Mikromasch, Tallinn, Estonia).

Image post-processing and analysis were performed using the Gwyddion analysis software [14]. The Gray-Level Co-occurrence Matrix (GLCM) features were extracted using the scikit package on Python version 3.8.10.

3. Results and Discussions

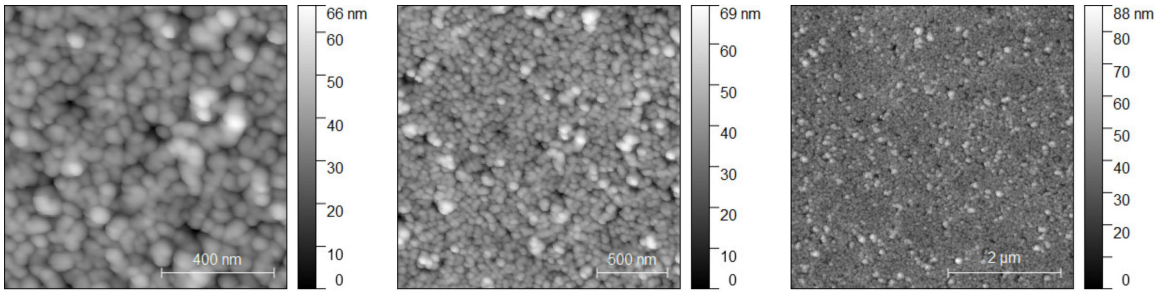
3.1. Surface Characterization

The AFM topography images of the nanoporous copper (NPC) films depicted in Figures 1 and 2 offer valuable insights into the surface characteristics of NPC 1 and NPC 2 films, scanned at three different scales. These images reveal distinct differences in their surface topography and suggest underlying mechanisms for these disparities.



(**a**) (**b**) (**c**)

Figure 1. AFM topography for NPC 1 for scanning square areas of (**a**) 1 × 1 µm, (**b**) 2 × 2 µm, and (**c**) 5 × 5 µm.



(**a**) (**b**) (**c**)

Figure 2. AFM topography for NPC 2 for scanning square areas of (**a**) 1 × 1 µm, (**b**) 2 × 2 µm, and (**c**) 5 × 5 µm.

On the smallest scanning scale of 1 × 1 µm (Figures 1a and 2a), both NPC 1 and NPC 2 films display nanoscale pore channels, indicating the successful completion of the dealloying process. These channels are essential for the unique properties and applications of nanoporous materials.

Comparing the two materials, the most noticeable difference in surface topography is observed at larger scanning scales (2 × 2 µm and 5 × 5 µm) in Figures 1b,c and 2b,c. NPC 2 exhibits a more pronounced and nonuniform nanoporous structure in these larger scans, indicating that some copper has aggregated on its surface. In contrast, NPC 1 shows clear and uniform pore channels and little-to-no copper aggregation on the surface. It is intriguing to note that both films were dealloyed for the same duration, yet they exhibit these distinct surface features.

The enhanced nanoporous structure in NPC 2 may be attributed to the greater diffusion and aggregation of copper atoms compared to NPC 1. The mechanism behind this phenomenon can be explained by the competition between the dissolution of aluminum (Al) ions and copper (Cu) ions during the dealloying process. Typically, Al ions tend to dissolve at a higher rate than Cu ions. However, as the dealloying time increases, the presence of AlO_2^- ions in the electrolyte solution plays a crucial role. AlO_2^- ions inhibit the dissolution

of aluminum, thus allowing Cu atoms to diffuse and aggregate on the surface. This observation provides a reasonable explanation for the surface differences seen in NPC 2, where the presence of AlO_2^- ions effectively prolongs the dissolution of Al and encourages the aggregation of Cu atoms, resulting in a more pronounced nanoporous structure.

The comparative analysis of the AFM topography images of NPC 1 and NPC 2 films suggests that the surface differences are mainly due to the competition between Al and Cu ions during the dealloying process. The presence of AlO_2^- ions inhibits Al dissolution and encourages Cu atom aggregation, resulting in a more pronounced nanoporous structure in NPC 2. These findings shed light on the distinct surface characteristics of these materials and highlight the importance of understanding the underlying mechanisms to control and optimize the properties of nanoporous materials for various applications.

It is also important to note that the precursor film shown in Figure 3a displays none of the characteristics of the dealloyed samples. It does not show any nanopores, and the surface structure appears to be highly irregular.

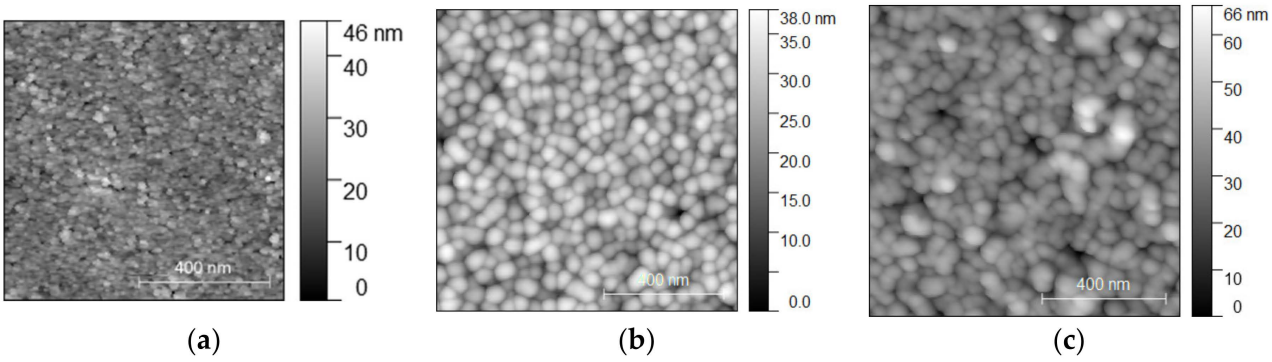


Figure 3. AFM topography for scanning square areas of 1 × 1 μm for (**a**) non-dealloyed, (**b**) NPC 1, and (**c**) NPC 2.

The compositions of the Cu–Al alloy precursor films were characterized by XRD. Figure 4 shows XRD patterns of the as-deposited $Cu_{25}Al_{75}$ precursor films. The peak position was calibrated through the comparison with the Si (100) peak whose position is 69.133 degree, and the 2-theta range of 25–67 degree is intercepted out as the peak of Si (100) substrates is too strong. XRD results illustrate that Al, AlCu, and $CuAl_2$ phases are observed in the as-deposited $Cu_{25}Al_{75}$ precursor films. Figures 5 and 6 show SEM images of the film surface and internal cross section of the NPC 1 and NPC 2 dealloyed films. They indicate that the NPC 2 film consists of irregular-shaped through-thickness columnar grains, while NPC 1 has a more regular surface.

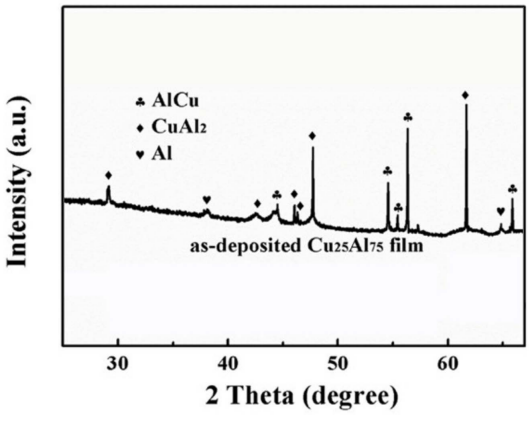
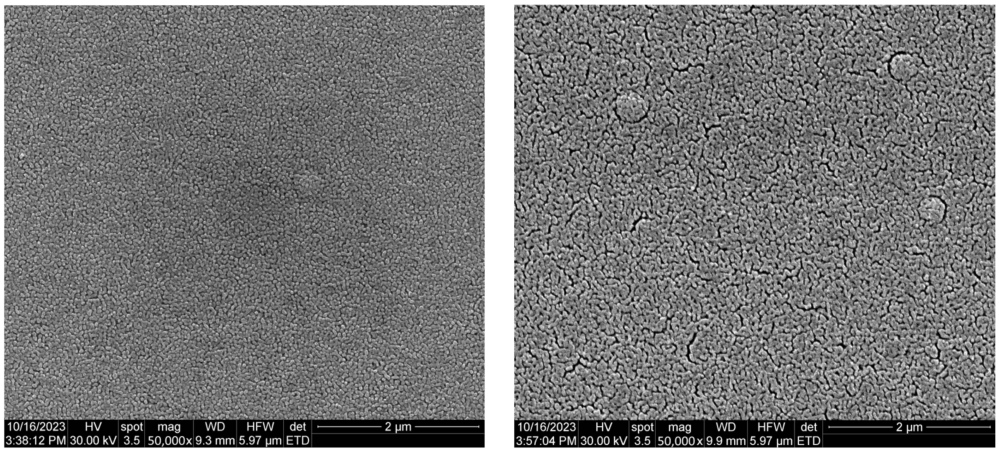
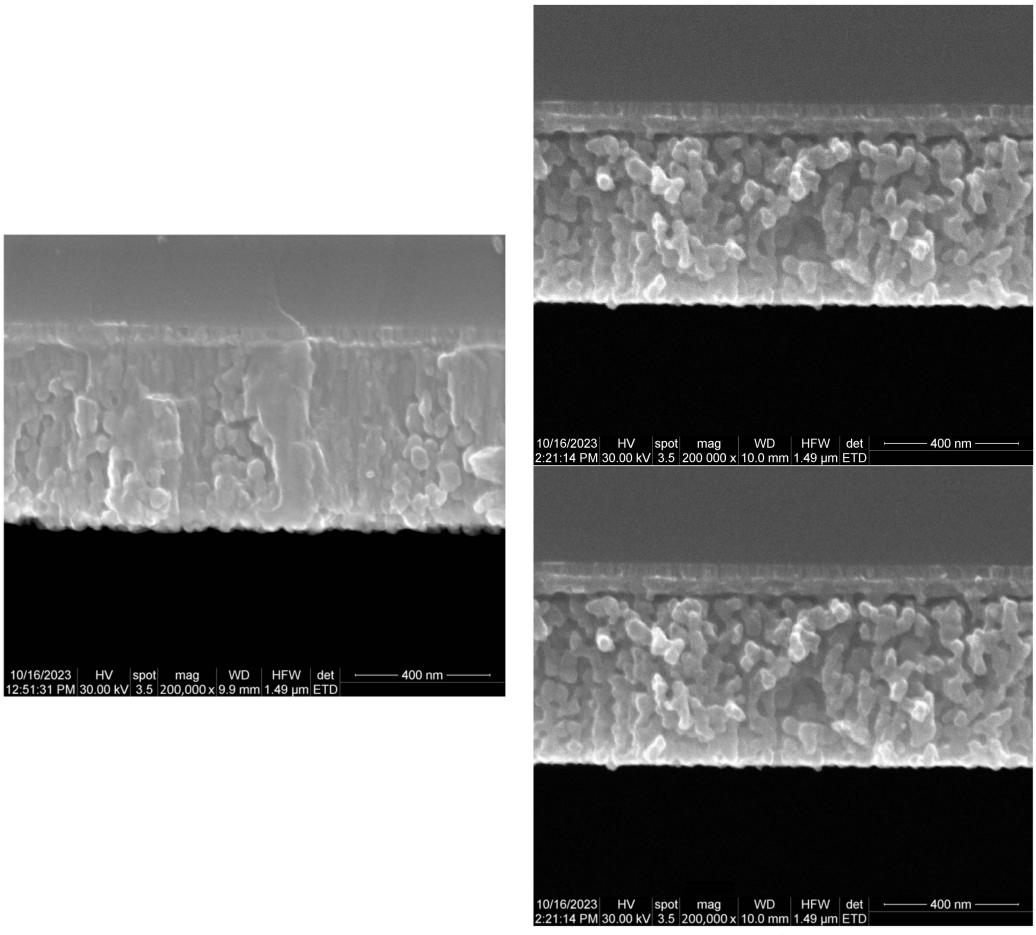


Figure 4. XRD patterns of the as-deposited $Cu_{25}Al_{75}$ precursor films.



(**a**) (**b**)

Figure 5. SEM film surface morphology for (**a**) NPC 1 and (**b**) NPC 2.



(**a**) (**b**)

Figure 6. SEM internal cross section for (**a**) NPC 1 and (**b**) NPC 2.

Concentrating on Figure 6, one can observe that for NPC 2 the dealloying process was more effective. In NPC 1, one can still see some structure of the precursor films.

This is confirmed by the EDX analysis on the NPC 1 and NPC 2 films (Figures 7 and 8), which indicates that almost no aluminum exists in the NPC 2 sample, which implies that most of the Al element is leached out from the precursor films during the etching process. For the NPC 1 sample, the Al peak is comparable size with the Cu peak, meaning that

the dealloying took place only for a limited depth near the contact surface, with little penetration inside the material.

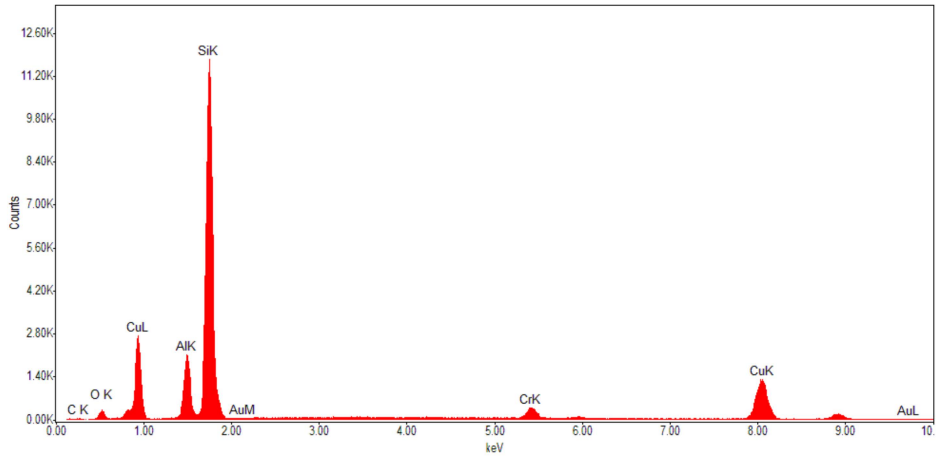


Figure 7. EDX characterization for the NPC 1 sample.

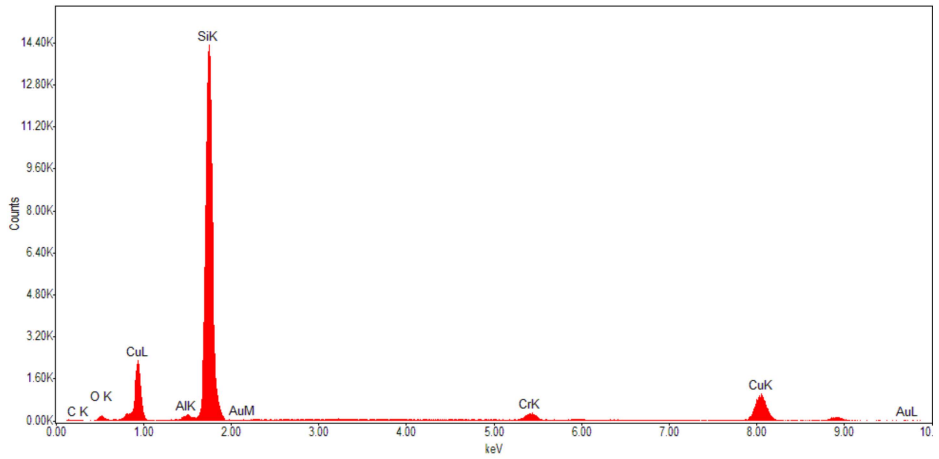


Figure 8. EDX characterization for the NPC 2 sample.

The use of fractal analysis in this study serves as a valuable tool to gain deeper insights into the structural complexity and self-similarity of NPC 1 and NPC 2 [15]. As mentioned earlier, both materials exhibited a similar type of nanoporous structure as the scanning area of the AFM images was increased, suggesting a potential underlying pattern of self-similarity that could be analyzed quantitatively.

The fractal analysis was conducted on the 1 × 1 µm AFM topography images using the triangulation method, and the results, as presented in Figure 9, revealed the fractal dimensions for NPC 1 and NPC 2 to be 2.51 and 2.44, respectively. These fractal dimensions serve as quantitative measures of the irregularity and complexity within the nanoporous structures.

The somewhat larger fractal dimension value of 2.51 for NPC 1 in comparison to the value of 2.44 for NPC 2 provides an interpretation of the structural differences between the two materials. A higher fractal dimension indicates a higher level of complexity and self-similarity within the structure. In the context of this study, a fractal dimension of 2.51 for NPC 1 suggests that its nanoporous structure is more intricate and exhibits a greater degree of self-similarity at different length scales. This could mean that NPC 1 has a more intricate and interconnected network of pores, leading to the observed larger fractal dimension.

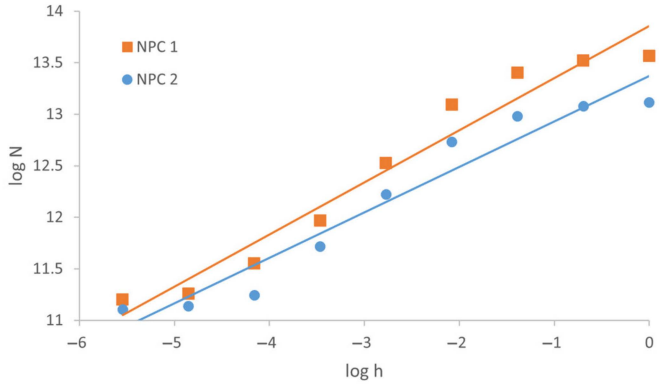


Figure 9. Fractal dimension of nanoporous copper NPC 1 (blue) and NPC 2 (orange).

Conversely, the fractal dimension of 2.44 for NPC 2 indicates a slightly lower level of structural complexity and self-similarity. It suggests that the nanoporous structure in NPC 2, although still exhibiting self-similarity, is somewhat less intricate and interconnected compared to NPC 1.

The extraction of pore size from the nanoporous materials NPC 1 and NPC 2 is a critical step in understanding the structural characteristics of these materials and how they are influenced by the choice of dealloying agents. This information provides valuable insights into the physical properties and potential applications of the materials.

The reason for extracting the pore size is that it serves as a fundamental parameter that can significantly impact the materials' properties and performance. Pore size is a key factor in determining the accessibility of the material's surface, its capacity for hosting guest molecules or ions, and its overall surface area. By analyzing pore size, we gain a better understanding of the materials' porosity and how it relates to their intended applications, such as in catalysis or filtration.

To extract the pore size, the thresholding method was employed, which is a widely accepted and effective technique for pore analysis. This method involves setting a specific height threshold in the AFM topography images, where areas with heights below the threshold are defined as pores. This enables a systematic and quantitative analysis of the pore size distribution.

Upon examining the results presented in Table 1, a clear and significant difference in pore size between NPC 1 and NPC 2 is evident. The films dealloyed in the NaOH solution exhibit pores that are approximately 39% larger than those dealloyed in H_2SO_4. This observation directly links the choice of dealloying agent to the resulting pore size, highlighting the critical role of the chemical environment in shaping the nanoporous structure. Larger pores in the NaOH-treated films can have important implications for applications such as ion transport, gas adsorption, or catalytic activity. This finding underscores the importance of understanding the relationship between processing conditions and the resulting material properties, providing valuable information for tailoring materials to specific applications.

Table 1. Pore size.

Sample	Pore Size (nm)
NPC 1	18 ± 6
NPC 2	25 ± 8

One reason for the larger pore size when using NaOH as the dealloying agent is the difference in the dissolution rates of the base metals in the alloys. NaOH is a strong alkali with a high pH, and it is known for its ability to rapidly dissolve certain metals, particularly aluminum. When the alloy is exposed to NaOH during the dealloying process, the aluminum component of the alloy is more readily and rapidly dissolved. This leads to the creation of larger voids or pores as the aluminum is leached away, leaving behind

interconnected spaces. In contrast, H_2SO_4 may not be as efficient at dissolving aluminum, resulting in smaller and less pronounced pores.

The extracted statistical quantities, including Ra, Sq, skew, kurtosis, surface area, and correlation length (Table 2), play a crucial role in characterizing and understanding the surface properties of nanoporous films, specifically in the context of nanoporous materials.

Table 2. Statistical quantities of the height distribution of the samples.

Measure	NPC 1	NPC 2
Ra (nm)	4.2 ± 0.1	5.7 ± 0.7
Sq (nm)	5.1 ± 0.1	7.4 ± 1.0
Skew (-)	-0.2 ± 0.1	0.02 ± 0.4
Excess Kurtosis (-)	-0.3 ± 0.1	0.7 ± 0.2
Surface area (μm^2)	1.1 ± 0.1	1.2 ± 0.1
Correlation length (nm)	7.6 ± 0.6	12.8 ± 1.1

Ra and Sq (Rugosity Measures): These parameters, Ra (average roughness) and Sq (root mean square roughness), provide insights into the surface roughness of the materials. In this case, it is observed that NPC 2, the material dealloyed with NaOH, exhibits higher rugosity compared to NPC 1, which was dealloyed with H_2SO_4. The slight difference in Ra and Sq, although on the order of nanometers, indicates that the surface of NPC 2 is somewhat rougher compared to NPC 1. This suggests that the use of NaOH as the dealloying agent leads to a slightly more textured and less smooth surface. This variation in surface roughness can be important in applications where adhesion, friction, or wettability plays a role.

Skew and Kurtosis (Height Distribution): Skewness and kurtosis provide information about the shape of the height distribution of the surface nano-topography. In this study, NPC 1 is characterized by being left-skewed and platykurtic, while NPC 2 is right-skewed and leptokurtic. These differences indicate that the height distribution on the surfaces of the two materials is fundamentally distinct. Left-skewness suggests a higher frequency of lower heights or valleys on the surface, while right-skewness implies a higher frequency of higher heights or peaks. Platykurtic distributions are flatter and have fewer extreme values, while leptokurtic distributions are more peaked and have more extreme values. These variations in height distribution may influence the surface's interaction with other substances, such as adsorption, capillarity, or mechanical properties, depending on the specific applications.

Surface Area: The discrepancy between the measured surface area and the projected surface area of 1 μm^2 is primarily due to the presence of the nanoporous structure on the sample surfaces. Both materials show similar surface areas, with differences attributed to the limitations in AFM resolution. This indicates that, from a macroscopic perspective, the two materials have a similar exposed surface area. However, the significant internal nanoporous structure contributes to the discrepancy.

Correlation Length: The correlation length provides information about the spatial arrangement and the extent of correlation between surface features. The distinguishable correlation length values for the two materials indicate that the choice of dealloying agent significantly influences the spatial distribution of surface features. A longer correlation length suggests a more extended arrangement of features that are correlated over larger distances, while a shorter correlation length implies a more compact or shorter-range arrangement. These differences in correlation length can have implications for various applications, such as surface adhesion, wetting, or electrical properties.

By using second-order statistical quantities such as the autocorrelation function (ACF), height–height correlation function (HHCF), and the power spectral density function (PSDF), we can analyze the relationship between points on the surface of the samples [13].

The ACF (Figures 10 and 11) provides insights into the correlation or similarity of surface features at different spatial separations. It quantifies the extent to which the height values at one point on the surface are correlated with the height values at another point. By analyzing the ACF, we can gain an understanding of how periodic or correlated the surface features are.

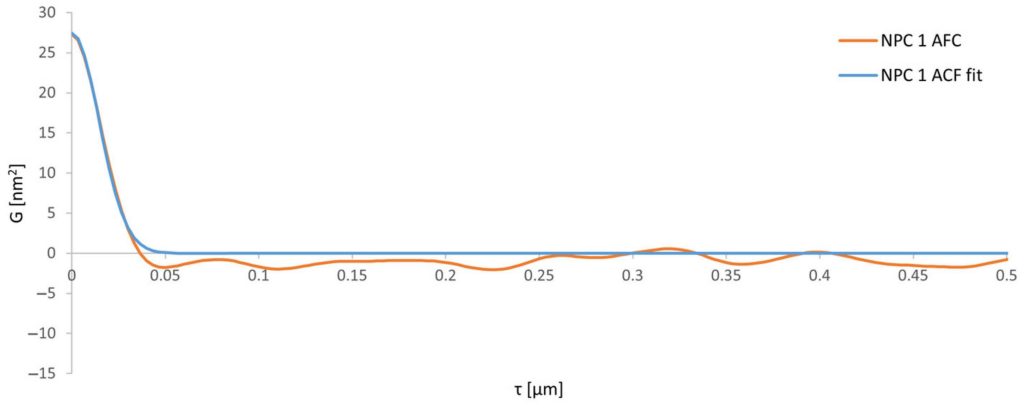


Figure 10. Autocorrelation function for NPC 1 (orange) and the Gaussian function fit (blue).

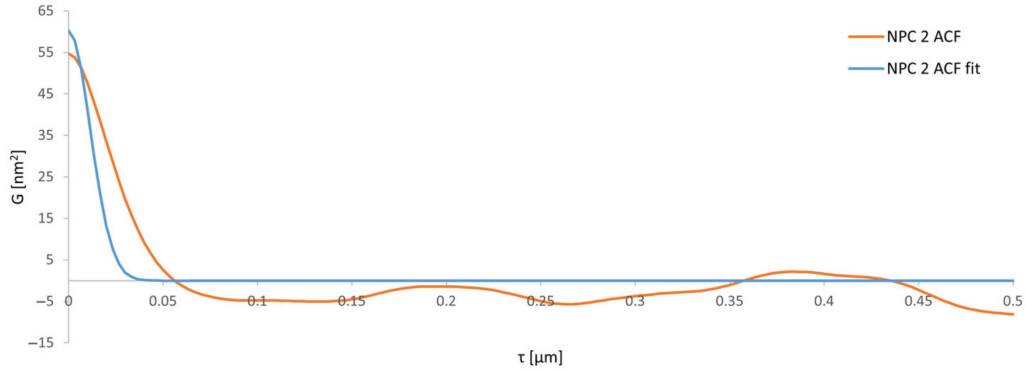


Figure 11. Autocorrelation function for NPC 2 (orange) and the Gaussian function fit (blue).

The HHCF (Figures 12 and 13) is a specialized form of the ACF, focusing on the correlation between the height fluctuations on the surface. It allows for a detailed examination of how height variations are correlated over different distances. The HHCF is particularly useful for assessing the statistical properties of surface roughness and fluctuations.

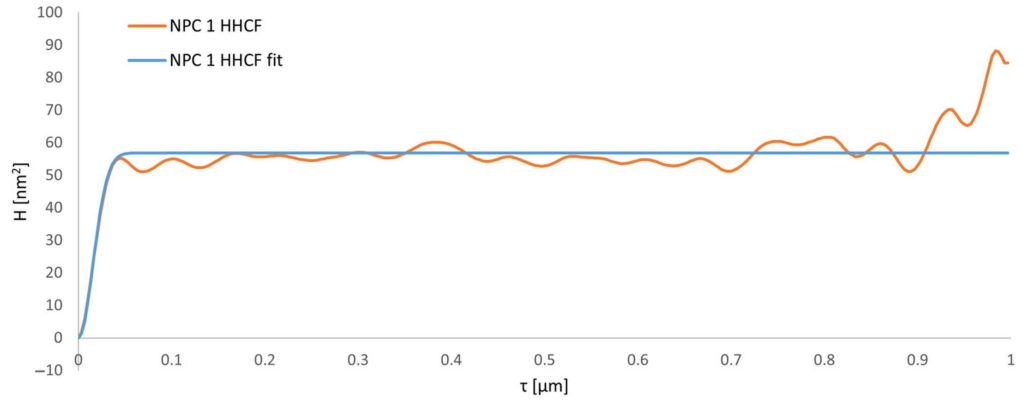


Figure 12. Height–height correlation function for NPC 1 (orange) and the Gaussian function fit (blue).

Fitting a Gaussian function on the ACF and HHCF graphs provides two important parameters for each sample: σ (root mean square deviation of the heights) and T (autocorrelation length).

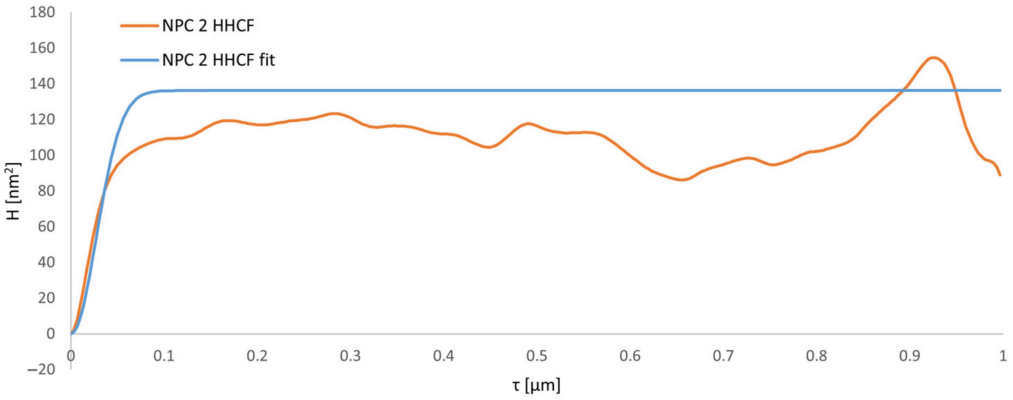


Figure 13. Height–height correlation function for NPC 2 (orange) and the Gaussian function fit (blue).

The σ and T values extracted from the four figures are shown in Table 3.

Table 3. Fit parameters for AFC and HHCF for the two samples.

Measure	σ (nm)	T (nm)
NPC 1 ACF	5.2	20.8
NPC 2 ACF	7.7	32.4
NPC 1 HHCF	5.3	21.2
NPC 2 HHCF	7.9	33.4

The values of σ, when compared for the same sample, show a high degree of similarity, as expected. This suggests that the root mean square deviation of heights is consistent within each material. It reflects the degree of surface roughness or height variation within the same sample, and the similarity indicates a level of consistency in surface characteristics.

The values of T, when compared for the same sample, are also almost the same, indicating a similar autocorrelation length within a material. Again, the consistency in T values for the same sample reaffirms that the spatial characteristics of the surface are maintained within each material.

The most important observation is the difference in the fitting parameters (σ and T) between the two materials, NPC 1 and NPC 2. This difference underscores the significant influence of the choice of dealloying solution on the mechanical properties of the samples. The unique values of σ and T for each material indicate that their surface roughness and the spatial arrangement of surface features are distinct. This information is vital for understanding how the materials will interact with their environment and how they might perform in applications where surface characteristics play a critical role, such as adhesion, friction, or wetting properties. The differences in these parameters between the two materials underscore the impact of the choice of dealloying solution on the materials' surface properties and their potential applications.

The power spectral density function (PSD) is a valuable tool for characterizing surface structures and periodicity. It provides information about how different spatial frequencies contribute to the overall roughness of a surface. In the context of this study, PSD is employed to assess the periodicity of the structures present on the surface of nanoporous films.

The PSD curve for NPC 1 in Figure 14 exhibits specific characteristics: a plateau followed by an inverse slope with a knee at the transition zone. The knee in the curve is observed at a spatial frequency of 0.0873 nm^{-1}. Despite NPC 1 being considered to have randomly rough surfaces, the PSD curve shows a peak at a spatial frequency of 0.0124 nm^{-1}.

The numerical interpretation of these results suggests that the knee point at 0.0873 nm^{-1} indicates a transition in surface roughness behavior. Above this point, there is no significant increase or decrease in roughness at low spatial frequencies, meaning that the surface roughness remains relatively constant and uncorrelated. The presence of a peak at 0.0124 nm^{-1}

indicates that there are some periodic structures on the surface of NPC 1. However, this peak is not well defined, implying that the periodic structures are not strongly dominant. In summary, the numerical analysis of the PSD for NPC 1 shows that, despite being categorized as having randomly rough surfaces, there are some weak periodic structures present. These structures are more prominent at lower spatial frequencies, while above the knee point, the roughness of the surface remains relatively uniform and uncorrelated.

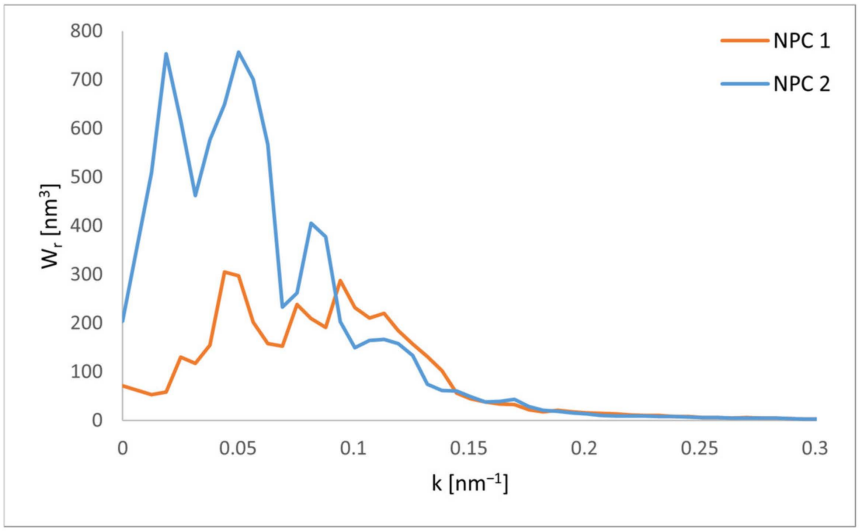


Figure 14. Power spectral density function for NPC 1 (orange) and NPC 2 (blue).

The PSD curve for NPC 2 in Figure 14 exhibits distinct features, including peaks at spatial frequencies of 0.0124 nm^{-1} and 0.0312 nm^{-1}.

The numerical interpretation of these results suggests that the presence of well-defined peaks at 0.0124 nm^{-1} and 0.0312 nm^{-1} indicates a strong periodicity in the surface structure of NPC 2. The presence of multiple peaks at different spatial frequencies suggests that NPC 2 exhibits more complex and organized surface features, with several periodic structures contributing to the overall roughness.

Minkowski connectivity is employed in this study to explore the local geometric and spatial structures of the nanoporous materials NPC 1 and NPC 2. This technique allows for a detailed examination of the spatial distribution of nanopores, with a focus on connectedness and topological characteristics. Minkowski connectivity is particularly sensitive to topological transformations in spatial arrangements, making it an effective tool for distinguishing between diverse morphologies. By applying this metric, we aim to differentiate and compare the characteristics of nanoporous copper obtained through the two different dealloying methods.

From the Minkowski connectivity curve in Figure 15, several observations can be made. The curve for both NPC 1 and NPC 2 exhibits oscillations, indicating variations in the connectedness and topological characteristics of the nanoporous structures as a function of spatial position (*z*-axis). These oscillations reflect the complex spatial distribution of pores and the changing connectivity of the nanoporous features.

The Minkowski connectivity values oscillate between negative and positive ranges for both materials. Negative values occur in the ranges of 0.967–0.997 µm for NPC 2 and 1.162–1.185 µm for NPC 1. These negative values suggest a predominance of valleys within these spatial intervals. The minimum negative value corresponds to the maximum density of valleys. Positive values are observed in the intervals of 0.997–1.030 µm for NPC 2 and 1.185–1.199 µm for NPC 1. These positive values indicate a predominance of peaks, with the maximum positive value denoting the maximum density of peaks.

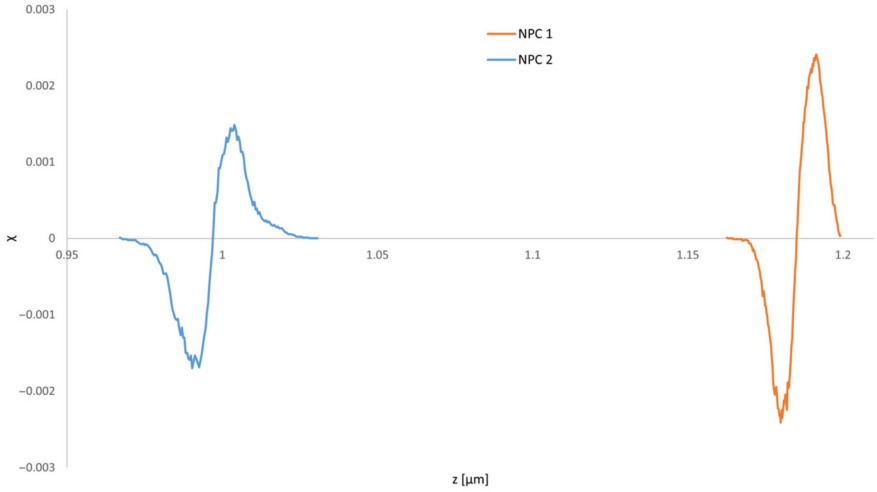


Figure 15. Minkowski connectivity for NPC 1 (orange) and NPC 2 (blue).

The identification of the maximum densities of peaks and valleys provides valuable insights into the surface properties based on topological results. The presence of peaks and valleys on the nanoporous surfaces can be indicative of various characteristics, such as roughness, spatial distribution, and connectivity. These topological characteristics can be critical for applications where surface properties play a significant role, such as adhesion, wettability, or the interaction of surfaces with other materials.

The features analyzed in Figure 16, including Angular Second Momentum (ASM), Contrast, Correlation, Dissimilarity, Energy, and Homogeneity, are extracted from Gray-Level Co-occurrence Matrix (GLCM) computations on the topography images. These features are employed for a statistical analysis of the surface characteristics. The GLCM matrix provides information about the spatial relationships of pixel values in the image, which is valuable for understanding the textural properties of the nanoporous materials. The reason for using these features is to quantify and compare the textural characteristics of materials NPC 1 and NPC 2 and how they are influenced by the choice of dealloying agent.

Variations Based on Dealloying Agent: The features, including ASM, contrast, dissimilarity, energy, and homogeneity, do not exhibit significant variations based on pixel distance. However, they do vary considerably depending on the dealloying agent used. This suggests that the choice of dealloying agent plays a critical role in shaping the textural characteristics of the nanoporous films. Each of these measures shows a clear distinction between NPC 1 (dealloyed in H_2SO_4) and NPC 2 (dealloyed in NaOH).

To differentiate between the resulting nanoporous surfaces obtained from the two dealloying agents, the average values over the entire pixel distance interval were calculated for NPC 1 and NPC 2. These average values serve as effective discriminators, indicating that the textural properties are distinct and characteristic of each material.

In addition to the features mentioned, the analysis of correlation values extracted from the surface topography GLCM matrix reveals variations. For NPC 1, correlation is observed at pixel distances of 142 and 262, while NPC 2 shows correlation at pixel distances of 108 and 189. Correlation measures the linear dependency of gray levels on neighboring pixels, indicating the degree of similarity or correlation in the distribution of grains and pores on the surface of the nanoporous copper. The variations in correlation values at different pixel distances suggest differences in the spatial arrangement and organization of surface features for NPC 1 and NPC 2.

The analysis of these features provides valuable insights into the textural characteristics of materials NPC 1 and NPC 2. These characteristics are strongly influenced by the choice of dealloying agent, and the distinctive patterns in ASM, contrast, dissimilarity, energy, homogeneity, and correlation values serve as robust indicators for discriminating between the two materials. These findings contribute to a deeper understanding of how the choice of

dealloying agent impacts the textural properties of nanoporous materials, which is essential for tailoring these materials for specific applications.

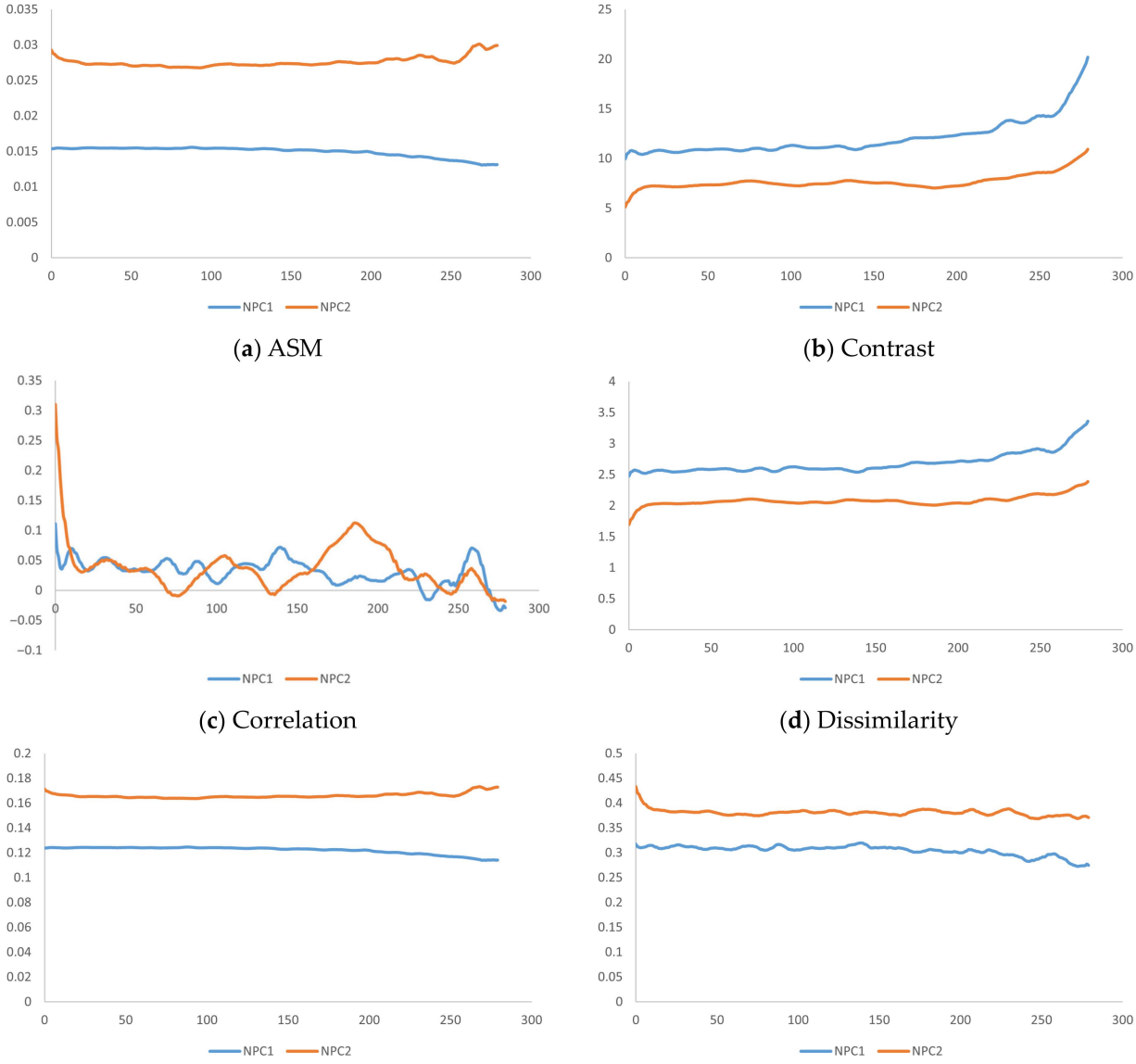


Figure 16. GLCM matrix features: (**a**) Angular Second Momentum (ASM), (**b**) Contrast, (**c**) Correlation, (**d**) Dissimilarity, (**e**) Energy, and (**f**) Homogeneity for NPC 1 (blue) and NPC 2 (orange).

As seen in Table 4, the best distinction between the two samples can be made using the GLCM ASM feature, as the value for NPC 2 is 1.92 times greater than the value for NPC 1. It is also worth noting that the contrast and dissimilarity features are the only ones that are greater for NPC 1 than NPC 2.

Table 4. GLCM matrix features.

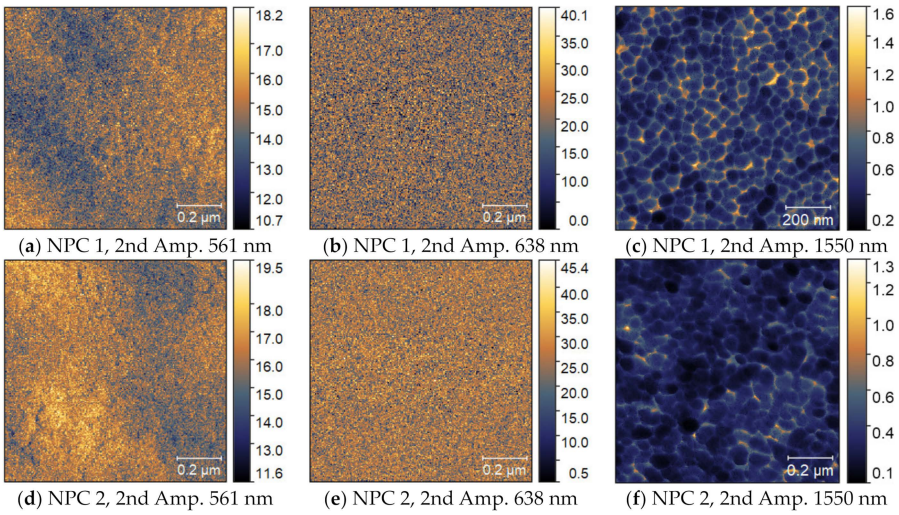
Sample	ASM	Contrast	Dissimilarity	Energy	Homogeneity
NPC 1	0.014	12.059	2.683	0.122	0.304
NPC 2	0.027	7.665	2.078	0.166	0.381

Regarding the ratio between the extracted features of the GLCM matrix, the energy feature is 1.36 times greater for NPC 2 than for NPC 1, and the homogeneity feature is 1.25 times greater for NPC 2 than for NPC 1. For the features where the extracted values are greater for NPC 1 than NPC 2, the ratios are 1.57 for the contrast feature and 1.29 for the dissimilarity feature.

3.2. Optical Near-Field Imaging and Analysis

s-SNOM investigations were performed at three different wavelengths in the VIS–NIR spectral range (561 nm, 638 nm, and 1550 nm). The scale bars of s-SNOM amplitude images are displayed in arbitrary units and cannot be compared across different wavelengths. However, for a given wavelength, the amplitude values exhibit a specific range, allowing for comparisons between two different samples. In s-SNOM phase images, the scale bars are expressed in radians.

Figure 17 displays the s-SNOM amplitude images of both NPC 1 and NPC 2 samples for the three investigated wavelengths. A low contrast is observed for 561 nm illumination (Figure 17a,d) for NPC 1 and NPC 2, respectively). The nano-sized grains are barely distinguishable, and there is a low contrast between extended areas. Assuming the connection between s-SNOM amplitude and reflectivity, we can conclude that the reflectivity of both samples shows minor variations at 561 nm.



(**a**) NPC 1, 2nd Amp. 561 nm (**b**) NPC 1, 2nd Amp. 638 nm (**c**) NPC 1, 2nd Amp. 1550 nm

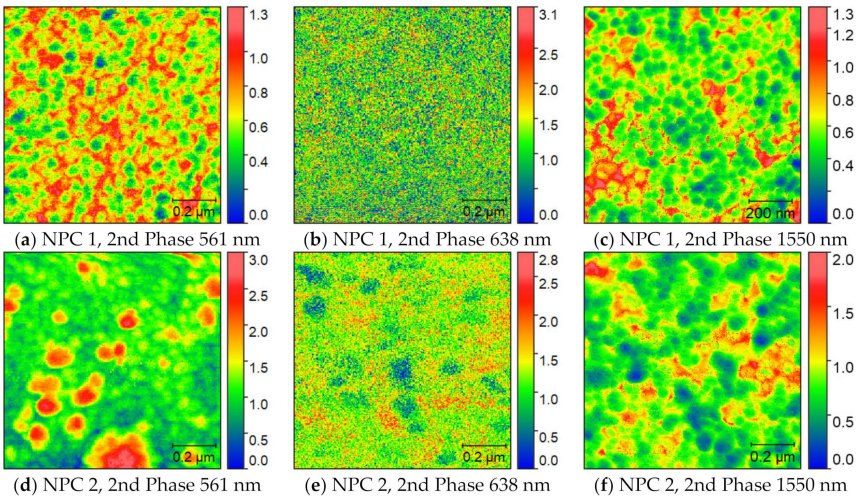
(**d**) NPC 2, 2nd Amp. 561 nm (**e**) NPC 2, 2nd Amp. 638 nm (**f**) NPC 2, 2nd Amp. 1550 nm

Figure 17. s-SNOM amplitude images for NPC 1 and NPC 2, for three different wavelengths: (**a**) NPC 1, 561 nm; (**b**) NPC 1, 638 nm; (**c**) NPC 1, 1550 nm; (**d**) NPC 2, 561 nm; (**e**) NPC 2, 638 nm; (**f**) NPC 2, 1550 nm.

For 638 nm illumination, the s-SNOM amplitude images (Figure 17b,e for NPC 1 and NPC 2, respectively) show no contrast resulting from Cu grains or pores. This indicates that the reflectivity of both samples at 638 nm is uniform. Interestingly, at a wavelength of 1550 nm (Figure 17c,f for NPC 1 and NPC 2, respectively), a high contrast is observed between Cu nanograins and their boundaries, potentially corresponding to pores or ligaments of the nanoporous structure. In sample NPC 1, the contrast is significantly higher than in the case of NPC 2.

The images corresponding to the s-SNOM phase information are displayed in Figure 18. In the case of s-SNOM investigations with 561 nm laser wavelength illumination (Figure 18a,d for NPC 1 and NPC 2, respectively), a clear contrast is observed between nanograins and pores. This result can be attributed to the typical absorption peak of Cu, which occurs near the 561 nm wavelength. An interesting observation is related to the image contrast: while in the case of NPC 1, the phase corresponding to the grains is lower than the phase corresponding to the pores, in the case of the NPC 2 sample, the phase contrast is reversed.

This effect may be linked to differences in ligament formation, which depend on the dealloying process.



(**a**) NPC 1, 2nd Phase 561 nm (**b**) NPC 1, 2nd Phase 638 nm (**c**) NPC 1, 2nd Phase 1550 nm

(**d**) NPC 2, 2nd Phase 561 nm (**e**) NPC 2, 2nd Phase 638 nm (**f**) NPC 2, 2nd Phase 1550 nm

Figure 18. s-SNOM phase images for NPC 1 and NPC 2, for three different wavelengths: (**a**) NPC 1, 561 nm; (**b**) NPC 1, 638 nm; (**c**) NPC 1, 1550 nm; (**d**) NPC 2, 561 nm; (**e**) NPC 2, 638 nm; (**f**) NPC 2, 1550 nm.

The differences between the two samples are highlighted by the s-SNOM phase images obtained at 638 nm (Figure 18b,e for NPC 1 and NPC 2, respectively). This time, for NPC 1, no contrast is observed in the phase image, indicating a uniform optical absorption at this wavelength. However, in the case of the NPC 2 sample, a small yet easily noticeable contrast is present between grains and pores, indicating a red-shifted optical absorption peak in the visible range compared to NPC 1.

In the case of s-SNOM investigations with a 1550 nm wavelength laser beam (Figure 18c,f for NPC 1 and NPC 2, respectively), a high contrast is observed between grains and holes, with the phase for both samples being lower for grains than for holes. While an absorption band in the NIR range is not characteristic of Cu, different nanostructured Cu particles, rods, or other engineered nano-sized structures can have absorption bands that can be tuned to NIR wavelengths [14].

3.3. Influence Factors

The specific mechanisms responsible for the observed differences in the mechanical and optical properties of nanoporous copper films dealloyed using different agents can be attributed to several factors.

Firstly, pore size plays a significant role. The choice of dealloying agent affects the dissolution rates of copper and aluminum, which are the constituent metals in the precursor films. Corrosive solutions like H_2SO_4 and NaOH exhibit different chemical reactivities towards these metals, resulting in varying dissolution rates. Faster dissolution of aluminum compared to copper in H_2SO_4 leads to smaller pores, while slower dissolution of aluminum in NaOH results in larger pore sizes.

Secondly, the dealloying agent influences the surface topography of the nanoporous copper films. The competition between the dissolution of aluminum and copper affects the redistribution and aggregation of copper atoms on the film surface. In the case of NaOH dealloying, more copper atoms diffuse and aggregate, leading to variations in surface features and the formation of agglomerations. These factors contribute to changes in the overall surface topography and roughness of the films.

Moreover, the dealloying process affects the formation of grains and ligaments within the nanoporous structure. The dissolution and redistribution of aluminum and copper atoms lead to the growth and coalescence of individual grains and ligaments. Different dealloying agents can result in variations in the size, shape, and arrangement of these grains and ligaments, thereby influencing the mechanical and optical properties of the films.

In terms of optical properties, the presence of different grain and ligament structures can impact the optical absorption of the nanoporous copper films. The absorption of light depends on the material's electronic band structure, which is influenced by the size, shape, and composition of the grains and ligaments. Variations in the arrangement and distribution of these structures can lead to differences in the absorption spectra and optical properties, particularly at specific wavelengths.

Additionally, nanoporous copper films exhibit plasmonic properties, which are highly sensitive to the local environment and surface morphology. The arrangement and size of the nanopores, as well as the presence of agglomerated copper atoms, can influence the surface plasmon resonance behavior. Consequently, this affects the optical properties, including reflectivity and phase contrast, observed in s-SNOM measurements.

Overall, the differences in the mechanical and optical properties of nanoporous copper films dealloyed using different agents arise from variations in pore size, surface topography, grain and ligament formation, optical absorption properties, and plasmonic effects. The choice of dealloying agent influences the dissolution kinetics, leading to different structural and compositional characteristics, which ultimately determine the observed differences in the properties of the films.

4. Conclusions

The article focuses on the investigation of nanoporous metals (NPMs), specifically nanoporous copper (NPC), for their applications in energy storage, catalysis, and surface-enhanced Raman scattering spectroscopy (SERS). The study aims to understand the optical properties and surface characteristics of NPC films that were dealloyed using different corrosive solutions.

The work also addresses the lack of investigation into the optical properties of NPC films, particularly using optical microscopy techniques. We utilized Atomic Force Microscopy (AFM) and scattering Scanning Near-field Optical Microscopy (s-SNOM) to examine the surface topography and optical characteristics of the NPC films. The AFM analysis revealed nanoscale pore channels in the NPC films, with variations depending on the dealloying agent used. The NPC films dealloyed in NaOH showed a more pronounced nanoporous structure compared to those dealloyed in H_2SO_4.

During the study, we employed various quantitative measurements and analysis techniques, such as fractal analysis, rugosity measures, correlation length determination, and Minkowski connectivity analysis, to characterize the surface properties of the NPC films. These analyses provided insights into parameters like pore size, complexity, rugosity, inclination angles, surface area, and correlation length, allowing for a comparative investigation between the NPC films dealloyed using different agents.

The study also utilized s-SNOM to investigate the optical properties of the NPC films at different wavelengths in the visible and near-infrared range. The s-SNOM amplitude and phase images provided information about the reflectivity, absorption, and contrast of the NPC films. The results indicated variations in reflectivity and optical absorption properties depending on the dealloying agent used, and the phase images revealed contrasts between grains and pores, which could be linked to differences in ligament formation during the dealloying process.

Overall, this work is important because it contributes to the understanding of the optical properties and surface characteristics of NPC films, shedding light on their potential applications in SERS, catalysis, and energy storage. The comparative investigation between NPC films dealloyed using different agents provides valuable insights for optimizing the fabrication process and tailoring the properties of nanoporous metals for specific applications.

Author Contributions: Conceptualization, S.R.A. and G.A.S.; data curation, S.R.A., D.E.T., R.H. and Z.H.; formal analysis, S.R.A. and R.H.; funding acquisition, C.K.B., E.F. and G.A.S.; investigation, S.R.A., D.E.T. and E.V.; methodology, D.E.T., Z.H. and G.A.S.; project administration, E.F. and G.A.S.; resources, E.F. and G.A.S.; software, S.R.A. and D.E.T.; supervision, C.K.B.; validation, S.G.S. and G.A.S.; visualization, S.R.A. and D.E.T.; writing—original draft, S.R.A. and D.E.T.; writing—review and editing, S.G.S., R.H., E.F. and G.A.S. All authors have read and agreed to the published version of the manuscript.

Funding: This work was supported by the UEFISCDI grant PN-III-P4-PCE-2021-0444 (RESONANO) and by the Exchanges Project at the 43rd Regular Meeting of the China-Romania Science and Technology Cooperation Committee and National Natural Science Foundation of China (11975034). The use of the Neaspec NeaSNOM Microscope was possible due to the European Regional Development Fund through Competitiveness Operational Program 2014–2020, Priority axis 1, Project No. P_36_611, MySMIS code 107066-INOVABIOMED.

Institutional Review Board Statement: Not applicable.

Informed Consent Statement: Not applicable.

Data Availability Statement: The data presented in this study are available on request from the corresponding author.

Conflicts of Interest: The authors declare no conflict of interest.

References

1. Qiu, H.-J.; Wang, J.; Liu, P.; Wang, Y.; Chen, M. Hierarchical nanoporous metal/metal-oxide composite by dealloying metallic glass for high-performance energy storage. *Corros. Sci.* **2015**, *96*, 196–202. [CrossRef]
2. Guo, X.; Han, J.; Liu, P.; Chen, L.; Ito, Y.; Jian, Z.; Jin, T.; Hirata, A.; Li, F.; Fujita, T. Hierarchical nanoporosity enhanced reversible capacity of bicontinuous nanoporous metal based Li-O_2 battery. *Sci. Rep.* **2016**, *6*, 33466. [CrossRef] [PubMed]
3. Chen, L.Y.; Yu, J.S.; Fujita, T.; Chen, M.W. Nanoporous copper with tunable nanoporosity for SERS applications. *Adv. Funct. Mater.* **2009**, *19*, 1221–1226. [CrossRef]
4. Ge, X.; Chen, L.; Zhang, L.; Wen, Y.; Hirata, A.; Chen, M. Nanoporous metal enhanced catalytic activities of amorphous molybdenum sulfide for high-efficiency hydrogen production. *Adv. Mater.* **2014**, *26*, 3100–3104. [CrossRef] [PubMed]
5. Hu, Y.-S.; Guo, Y.-G.; Sigle, W.; Hore, S.; Balaya, P.; Maier, J. Electrochemical lithiation synthesis of nanoporous materials with superior catalytic and capacitive activity. *Nat. Mater.* **2006**, *5*, 713–717. [CrossRef] [PubMed]
6. Hu, Z.; Wang, J.; Li, R.; Xu, C.; Liu, X.; Wang, Y.; Fu, E.; Lu, Z. Ion irradiation-enhanced raman scattering on nanoporous copper. *Langmuir* **2018**, *34*, 13041–13046. [CrossRef] [PubMed]
7. Wang, J.; Hu, Z.; Li, R.; Liu, X.; Xu, C.; Wang, H.; Wu, Y.; Fu, E.; Lu, Z. Influences of Au ion radiation on microstructure and surface-enhanced Raman scattering of nanoporous copper. *Nanotechnology* **2018**, *29*, 184001. [CrossRef] [PubMed]
8. Mubeen, S.; Lee, J.; Singh, N.; Krämer, S.; Stucky, G.D.; Moskovits, M. An autonomous photosynthetic device in which all charge carriers derive from surface plasmons. *Nat. Nanotechnol.* **2013**, *8*, 247–251. [CrossRef] [PubMed]
9. Chan, L.-H.; Yasuda, K.; Song, J.-M.; Suga, T. Hydrophilic nanoporous copper surface prepared by modified formic acid vapor treatment. *Surf. Interfaces* **2022**, *28*, 101620. [CrossRef]
10. Ji, Y.; Xing, Y.; Zhou, F.; Li, X.; Chen, Y.; Shao, L.H. The mechanical characteristics of monolithic nanoporous copper and its composites. *Adv. Eng. Mater.* **2018**, *20*, 1800574. [CrossRef]
11. Bai, Q.; Zhang, C.; Tan, F.; Wu, F.; Zhang, Z. Nanoporous copper as an inexpensive electrochemical actuator responsive to sub-volt voltages. *Electrochem. Commun.* **2021**, *124*, 106940. [CrossRef]
12. Koya, A.N.; Zhu, X.; Ohannesian, N.; Yanik, A.A.; Alabastri, A.; Proietti Zaccaria, R.; Krahne, R.; Shih, W.-C.; Garoli, D. Nanoporous metals: From plasmonic properties to applications in enhanced spectroscopy and photocatalysis. *ACS Nano* **2021**, *15*, 6038–6060. [CrossRef] [PubMed]
13. Mao, R.; Liang, S.; Wang, X.; Yang, Q.; Han, B. Effect of preparation conditions on morphology and thermal stability of nanoporous copper. *Corros. Sci.* **2012**, *60*, 231–237. [CrossRef]
14. Nečas, D.; Klapetek, P. Gwyddion: An open-source software for SPM data analysis. *Open Phys.* **2012**, *10*, 181–188. [CrossRef]
15. Ibrahim, S.; Dworzak, A.; Crespo, D.; Renner, F.U.; Dosche, C.; Oezaslan, M. Nanoporous copper ribbons prepared by chemical dealloying of a melt-spun ZnCu alloy. *J. Phys. Chem. C* **2021**, *126*, 212–226. [CrossRef]

Disclaimer/Publisher's Note: The statements, opinions and data contained in all publications are solely those of the individual author(s) and contributor(s) and not of MDPI and/or the editor(s). MDPI and/or the editor(s) disclaim responsibility for any injury to people or property resulting from any ideas, methods, instructions or products referred to in the content.